Melting of Lennard-Jones rare-gas clusters doped with a single impurity atom

Nicolás Quesada
Instituto de Física, Universidad de Antioquia, AA 1226 Medellín, Colombia

Gloria E. Moyano*
Instituto de Química, Universidad de Antioquia, AA 1226 Medellín, Colombia

(Received 10 May 2010; revised manuscript received 13 July 2010; published 10 August 2010)

The single impurity effect on the melting process of magic number Lennard-Jones rare gas clusters of up to 309 atoms is studied on the basis of parallel tempering Monte Carlo simulations in the canonical ensemble. A decrease on the melting temperature range is prevalent, although such an effect is dependent on the size of the impurity atom relative to the cluster size. Additionally, the difference between the atomic sizes of the impurity and the main component of the cluster should be considered. We demonstrate that solid-solid transitions due to migrations of the impurity become apparent and are clearly differentiated from the melting up to cluster sizes of 147 atoms.

DOI: 10.1103/PhysRevB.82.054104 PACS number(s): 36.40.Ei, 61.46.−w

I. INTRODUCTION

Alloying effects in atomic nanoclusters cover a domain of property behavior wider and more complex than those corresponding to individual atoms and bulk matter, with strong particle size specificities which combine with composition and finite-size effects. Even for pure substances, the structure of their atomic nanoclusters is very dependent on the number of atoms per particle. There are "magic" numbers, corresponding to cluster structures characterized by their conspicuous energetic stabilities relative to size but for a given finite cluster structure, stability results from a trade-off between packing and surface effects. General nonmonotonic property trends as a function of size characterize finite clusters so complex structural transitions may occur during the growth from finite sizes to the bulk. The addition of dopant atoms to a pure atomic cluster can alter its structure and growth patterns depending on the nature of both the impurity and the cluster, the cluster size, and the concentration of dopant atoms. The possibility to manipulate nanoparticle structures and so, tune their physicochemical properties (e.g., catalytic, electronic, thermodynamic) has motivated a lot of recent research on alloy nanoclusters.[1,2]

Regarding the phase changes, the melting process of pure and alloy clusters has attracted considerable attention in experimental as well as in theoretical studies. A number of specific features have been recognized in the melting mechanisms of finite particles such as solid-solid structure changes prior to melting,[3] *premelting*[2] effects of surface loosening (formation of "liquidlike" surface layers[4,5]), coexistence of different atom-packing schemes,[6] oscillations between the liquid and solid phases,[7] etc.

The melting temperature as a function of the cluster size has been studied on the basis of several models which agree on predicting that the melting temperature decreases linearly or quasilinearly with the inverse of the radius of the particle.[2,8,9] The pioneering work by Pawlow is summarized in the formula,

$$T_M(N) = T_M(\infty)(1 - CN^{-1/3})$$

in which $T_M(N)$ and $T_M(\infty)$ represent the melting temperatures of a N-sized spherical cluster and the bulk, respectively; and C is a constant (see Ref. 2 for a derivation of this law and further correction terms). Pawlow's law is consistent with several experimental results and, although deviations occur for the smaller clusters, whose shapes are far from spherical, the melting point of nanoclusters is usually depressed. Nevertheless, there is experimental evidence of exceptions to this trend for cases like the ionic tin clusters with 10–30 atoms, whose melting points are at least 50 K above that of the bulk.[10] In addition to the size effects, the melting temperatures of alloy clusters can be increased[11] or decreased[12] with respect to those of the pure components.[1] The amount and direction of the shiftings of the melting point in finite doped atomic clusters can be attributed to several factors: alterations of the cluster structure, whether or not the impurity is soluble in the cluster, many-body energetic effects, and/or other complex energetic-entropic effects.[12]

The phenomenology seen in the melting mechanisms of pure clusters is also apparent for binary and multiple-component clusters but having the composition as an additional variable enormously increases the complexity of structural behaviors.[13,14] Alloying effects in mixed atomic clusters depend on the differences between the atomic sizes, cluster surface energies, overall structure strain, number and strength of the interactions between unlike atoms.[14] Further contributing aspects may be kinetic factors, specific electronic/magnetic effects, and environmental conditions.[1] Alloying effects can be significant even when a single impurity is introduced into a cluster on the order of a hundred atoms.[11]

An efficient scheme to model the melting of doped atomic clusters has to address the issues associated with the increased complexity of the energy landscapes to explore during the simulations of mixed clusters, the occurrence of homotop structures, as well as convergence difficulties related to quasiergodicity that have been described elsewhere.[15,16] Methods such as replica exchange molecular dynamics and parallel tempering Monte Carlo (PTMC) have been developed to address the quasiergodicity by improved sampling. PTMC is a powerful method to sample rugged energy surfaces which takes advantage of the fact that replicas running

TABLE I. Global minima for the different compositions considered, corresponding energies in absolute units $E_0/\epsilon_{\mathrm{Ar}}$, in units relative to their matrix composition E_0/ϵ_i, shell position of the dopant atom in the structure (number of shell containing the impurity/total number of shells in cluster, the zeroth shell is the geometric center of the icosahedron), point group, and the melting temperature of each cluster in kelvin.

Cluster	$E_0/\epsilon_{\mathrm{Ar}}$	E_0/ϵ_i	Dopant position	Point group	T_M/K
LJ_{13}	−44.3268	−44.3268		I_h	
$Ar_{12}Xe$	−47.6981	−47.6981	1/1	C_{5v}	30.22
$ArXe_{12}$	−78.6977	−42.4934	0/1	I_h	59.96
$Kr_{12}Xe$	−62.5139	−45.5132	1/1	C_{5v}	41.51
$KrXe_{12}$	−81.0895	−43.7848	0/1	I_h	62.74
LJ_{55}	−279.248	−279.248		I_h	
$Ar_{54}Xe$	−284.276	−284.276	2/2	C_{2v}	31.25
$ArXe_{54}$	−516.170	−278.709	0/2	I_h	63.78
$Kr_{54}Xe$	−386.018	−281.040	2/2	C_{2v}	42.93
$KrXe_{54}$	−517.631	−279.498	0/2	I_h	65.33
LJ_{147}	−876.461	−876.461		I_h	
$Ar_{146}Xe$	−882.335	−882.335	3/3	C_{3v}	42.33
$ArXe_{146}$	−1625.44	−877.667	0/3	I_h	79.86
$Kr_{146}Xe$	−1206.77	−878.584	3/3	C_{3v}	58.14
$KrXe_{146}$	−1625.44	−877.666	0/3	I_h	79.59
LJ_{309}	−2007.22	−2007.22		I_h	
$Ar_{308}Xe$	−2013.39	−2013.39	3/4	C_{3v}	50.18
$ArXe_{308}$	−3722.59	−2010.04	0/4	I_h	94.13
$Kr_{308}Xe$	−2760.16	−2009.53	3/4	C_{3v}	68.92
$KrXe_{308}$	−3721.20	−2009.28	0/4	I_h	93.06

at high temperature are able to sample most of the relevant configuration space. At the same time, through configuration exchange PTMC connects high-temperature replicas, which can visit most of the configuration space, with replicas at low temperatures so that the latter do not get trapped in local minima.[17]

The paper has been written as follows: In Sec. II, we present the methodology for optimal structure search, sampling and observable calculations to monitor the cluster melting process. Then, in Sec. III we discuss the features that differentiate the melting of doped clusters from that of the pure ones, taking into account their composition and cluster size. Special detail is given to the study of the low-temperature solid-solid transitions. Finally we present some general conclusions.

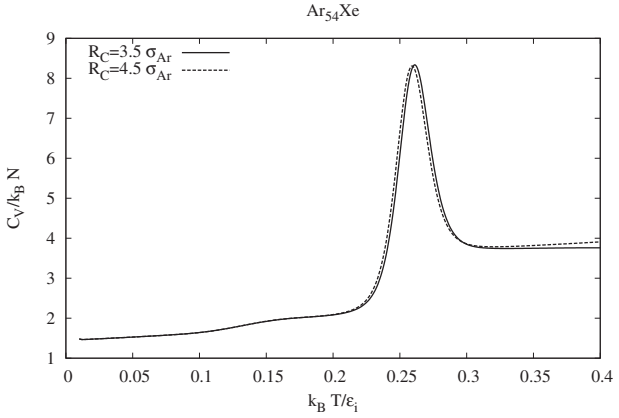

FIG. 1. Volume dependence of the C_V curve for $Ar_{54}Xe$.

II. METHODOLOGY

In this work, we used the scaled Lennard-Jones (LJ) parameters σ_i and ϵ_i for the rare gas interactions reported in Ref. 14.

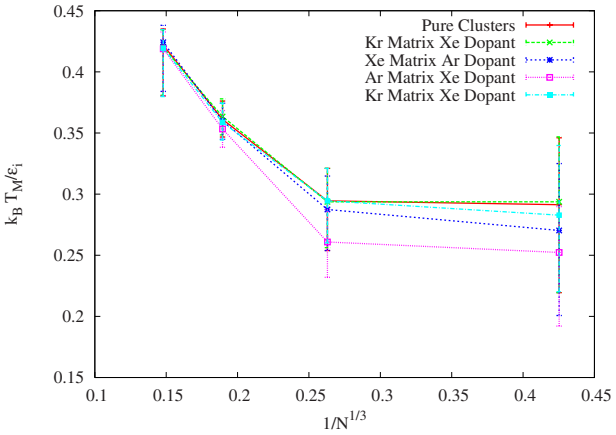

FIG. 2. (Color online) Melting temperatures (T_M) as a function of $N^{-1/3}$ for each type of composition studied. The bars represent the width of the peak associated with the melting of the cluster.

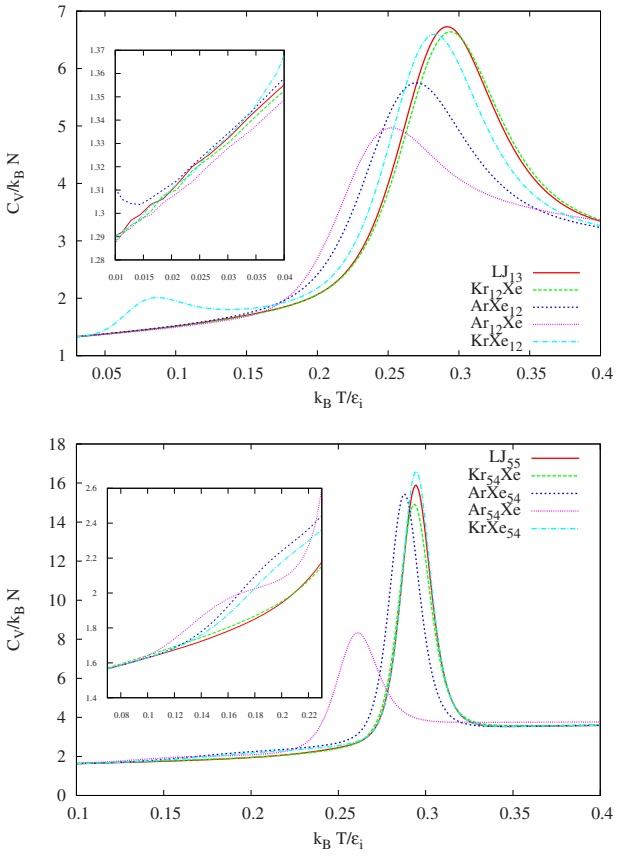

FIG. 3. (Color online) Constant volume heat capacities C_V as a function of temperature for cluster sizes 13 and 55.

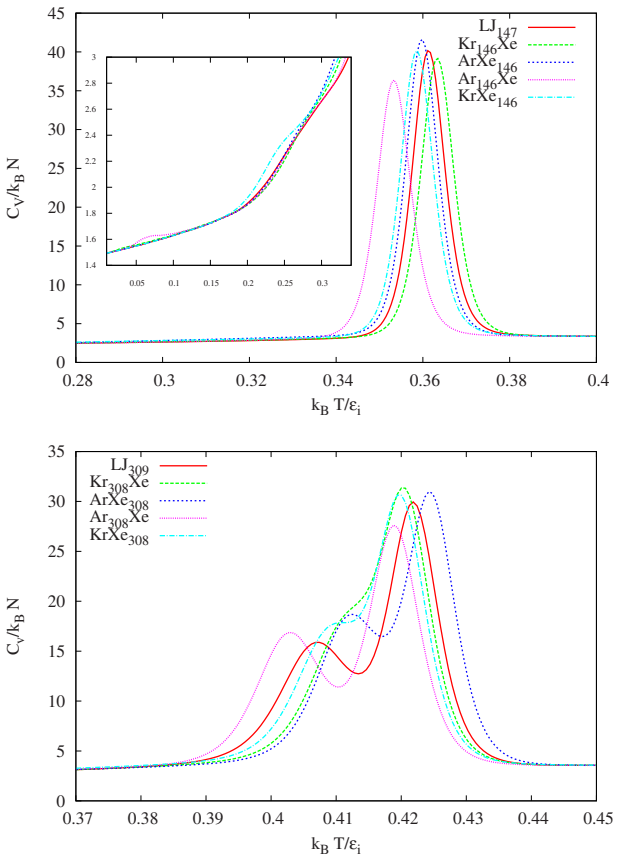

FIG. 4. (Color online) Constant volume heat capacities C_V as a function of temperature for cluster sizes 147 and 309.

A. Optimal structures

To obtain the (putative) global minima presented in Table I (excepting for the cases of the pure LJ clusters, the 13-atom clusters, $Ar_{54}Xe$ and $ArXe_{54}$ which had already been reported in Refs. 14 and 18) we performed three types of calculations:

(1) local optimizations using the Fletcher-Reeves conjugate gradient algorithm (FRCGA) were performed starting from the structures of the global minima of each pure cluster, in which one atom of the pure cluster was substituted by the dopant atom. This way we obtained a set of icosahedral low-energy structures.

(2) In a complementary, ampler search, we used the Basin-Hopping (BH) method.[19] To sample the energy surfaces, two types of random moves were performed: Moving all the atoms at the same time and swapping, the dopant atom with an atom of the matrix. We performed at least 20 000 steps (=swaps+moves) in which, after each move, we performed a local optimization using the FRCGA. For all the compositions, the BH method arrived to the same result of the first procedure.

(3) Additionally, after the finite-temperature simulations described in Sec. II B, we quenched samples saved at different temperatures for each composition. For the smallest clusters, we performed around 25 000 local minimizations, and for larger clusters about 55 000 local optimizations.

The results were equivalent for all procedures in the above list. We note that the first strategy was computationally much cheaper than the other two. The minima in Table I

TABLE II. Cluster sizes (N), number of temperatures simulated (n), their minimum (T_0) and maximum (T_f) values, constraining radii (R_c), number of Monte Carlo steps (N_{MC}) and frequencies at which swaps between adjacent replicas were attempted (N_{swap}). The constraining radii R_c and the temperatures T_0 and T_f are given in units of the LJ parameters of the atoms of the matrix.

N	n	k_BT_0/ϵ_i	k_BT_f/ϵ_i	R_c/σ_i	N_{MC}	N_{swap}
13	31	0.01	0.4	2.5	4×10^8	100
55	71	0.01	0.4	3.5	8×10^8	100
147	71	0.01 and 0.2	0.4 and 0.5	4.5	1.6×10^9	250
309	71	0.2	0.5	5.5	2×10^9	500

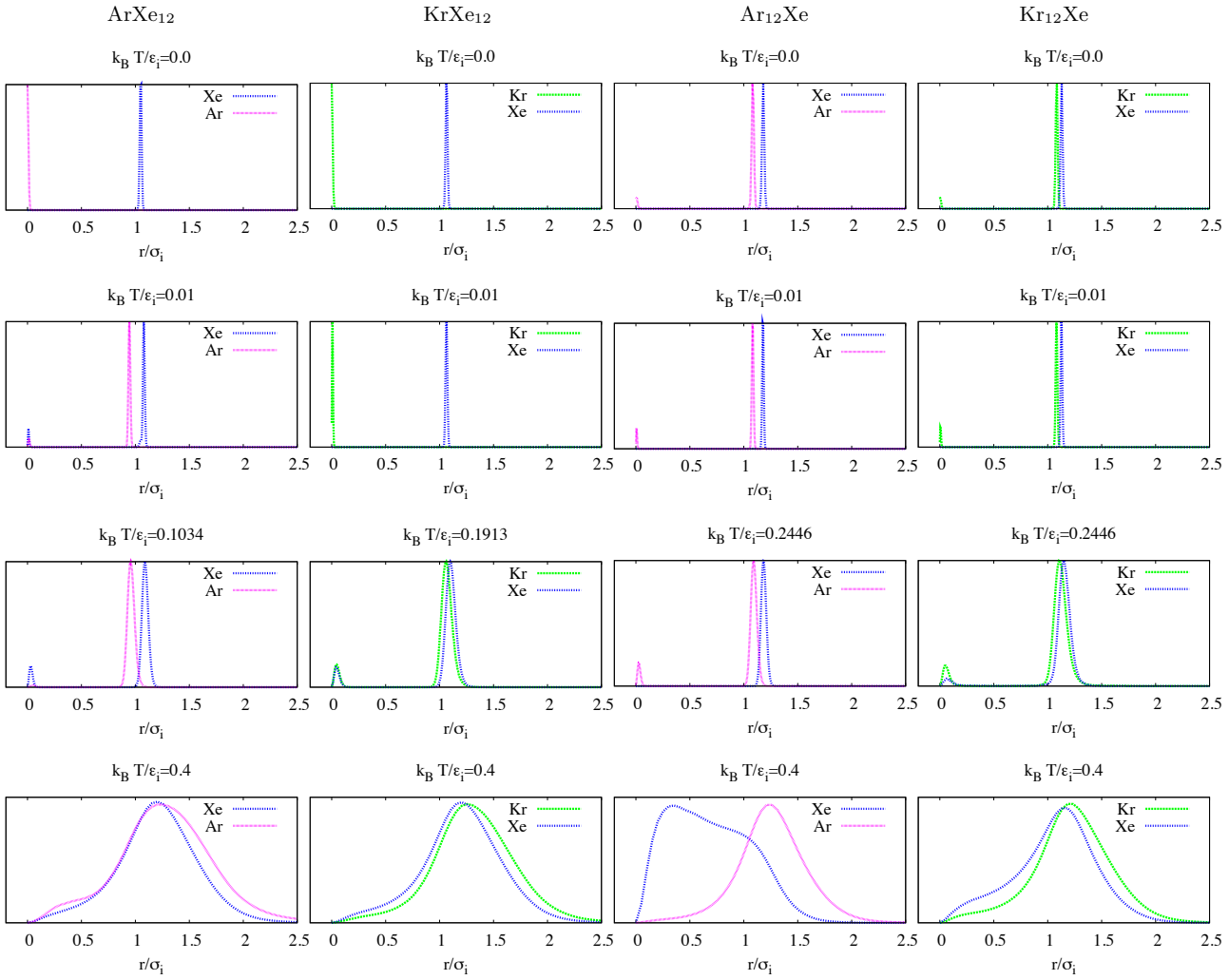

FIG. 5. (Color online) Radial distribution function for 13-atom clusters. The distribution of the figures is as follows: the columns correspond to the compositions $ArXe_{N-1}$, $KrXe_{N-1}$, $Ar_{N-1}Xe$, and $Kr_{N-1}Xe$. The top row of the panel shows the RDFs of the lowest energy structures. The bottom row contains the RDFs of the clusters once they have melted. The second and third rows correspond to intermediate temperatures of the melting range, illustrating the structural changes discussed in the text. This panel description applies also to Figs. 6–8.

were used to initialize the finite-temperature simulations.

Considering the lowest energy structures, the dopant atom takes the central position of the cluster when the impurity is Ar or Kr while it remains in one of the two most external shells when the impurity is Xe.

B. Sampling strategy

To sample the complex energy surfaces of our systems in the canonical ensemble, we used the PTMC method.[15] For each replica, we have used two types of moves. On the one hand, single-particle moves have been implemented using an adaptive step that assures that half of the time the new configuration will be accepted. On the other hand, since we have two different atomic species in each cluster, we have also implemented particle exchange moves. This sampling strategy consists in exchanging the position of two different atoms in the clusters. The simulation temperatures were chosen according to the geometric progression $T_i = T_0\lambda^i$. The number of temperatures for the simulations as well as their maximum and minimum values are summarized in Table II.

For each system, the number of equilibration steps was always equal to the number of Monte Carlo steps (N_{MC}). To prevent the evaporation of the clusters, we implemented hard sphere constraining potentials for the constraining radii listed in Table II.

Finally, the swapping acceptance ratios between replicas in all the systems simulated remained around 60–70 % and never went below 35%.

C. Observables

We analyze the melting process by monitoring various observables. First, the heat capacity C_V, which is calculated according to the formula,

$$C_V(T) = \frac{1}{k_B T^2}(\langle E^2\rangle_T - \langle E\rangle_T^2).$$

To interpolate the points obtained with the PTMC simulation and have a smooth dependence in the $C_V(T)$ curve, we used the multihistogram method.[20,21] Note that the formula given above depends on the volume in which the system is con-

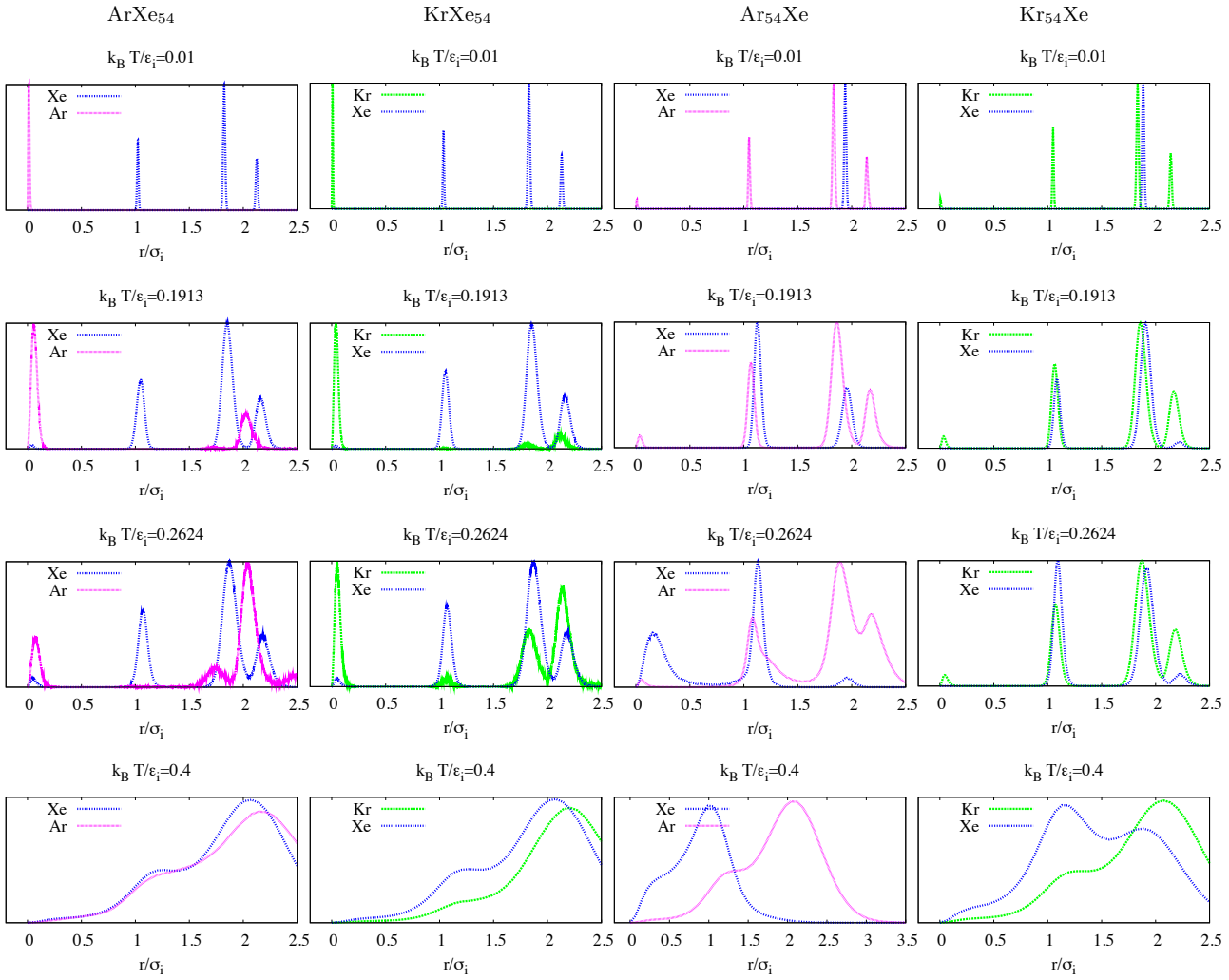

FIG. 6. (Color online) Radial distribution function for 55-atom clusters.

strained to move. In Fig. 1, we compare the $C_V(T)$ curves for two constraining volumes. Notice that although the second volume is twice the first $[V(R_C=4.5\sigma_{\mathrm{Ar}})/V(R_C=3.5\sigma_{\mathrm{Ar}}) \approx 2.13]$, the main peak is not strongly affected and the features of the curve below the main peak basically do not change (As one expects from a "solid" phase).

To monitor the effects of the dopant atom in each cluster, we calculated the radial distributions functions (RDFs) $g(r)$ of the dopant atom and of the rest of the atoms in the matrix, for these calculations all the distances r have been taken with respect to the *geometric* center of the cluster $\vec{r}_{geom}$, where $\vec{r}_{geom}=\frac{1}{N}\Sigma_i^N \vec{r}_i$, N represents the *total* number of atoms in the cluster.

To further quantify the delocalization of the atom, we calculated the standard deviation of the RDF of the dopant atom (ξ) according to

$$\xi = \sqrt{\langle r_{dopant}^2 \rangle - \langle r_{dopant} \rangle^2}.$$

D. Harmonic superposition method

To understand the solid-solid transitions that occur in a doped cluster between homotops, we have used the harmonic superposition method (HSM).[22,23]

This method assumes that there is a number m of well-defined states that make most of the contribution to the partition function in a certain range of temperatures. Then, one approximates the contribution of each state to the partition function $[Z(T)]$ as the contribution of its harmonic part. Such partition function is obtained from the normal modes and frequencies by expanding the potential around the corresponding minimum in a power series up to quadratic order,

$$V(\vec{R}) = V(\vec{R}_0) + \frac{1}{2}\vec{R}^T\hat{H}\vec{R} + \mathcal{O}(R^3),$$

where $\vec{R}=(\vec{r}_1,\ldots,\vec{r}_N)$, $\vec{R}_0$ is the equilibrium position and $\hat{H}$ is the Hessian Matrix of that minimum. To obtain the partition function (and the thermodynamics of the system), one adds the simple harmonic oscillator partition functions of each state,

$$Z(T) = \sum_{\alpha}^{m} n_\alpha \frac{\exp(-\beta E_\alpha)}{(\beta h \bar{\nu}_\alpha)^{3N-6}} = \sum_{\alpha}^{m} n_\alpha Z_\alpha(T),$$

where $\beta=1/k_BT$, E_α is the energy of each state, n_α is its degeneracy due to symmetry $[n_\alpha=2p!(N-p)!/h_\alpha$, N the number of atoms, p the number of impurities, $p=1$ and h_α

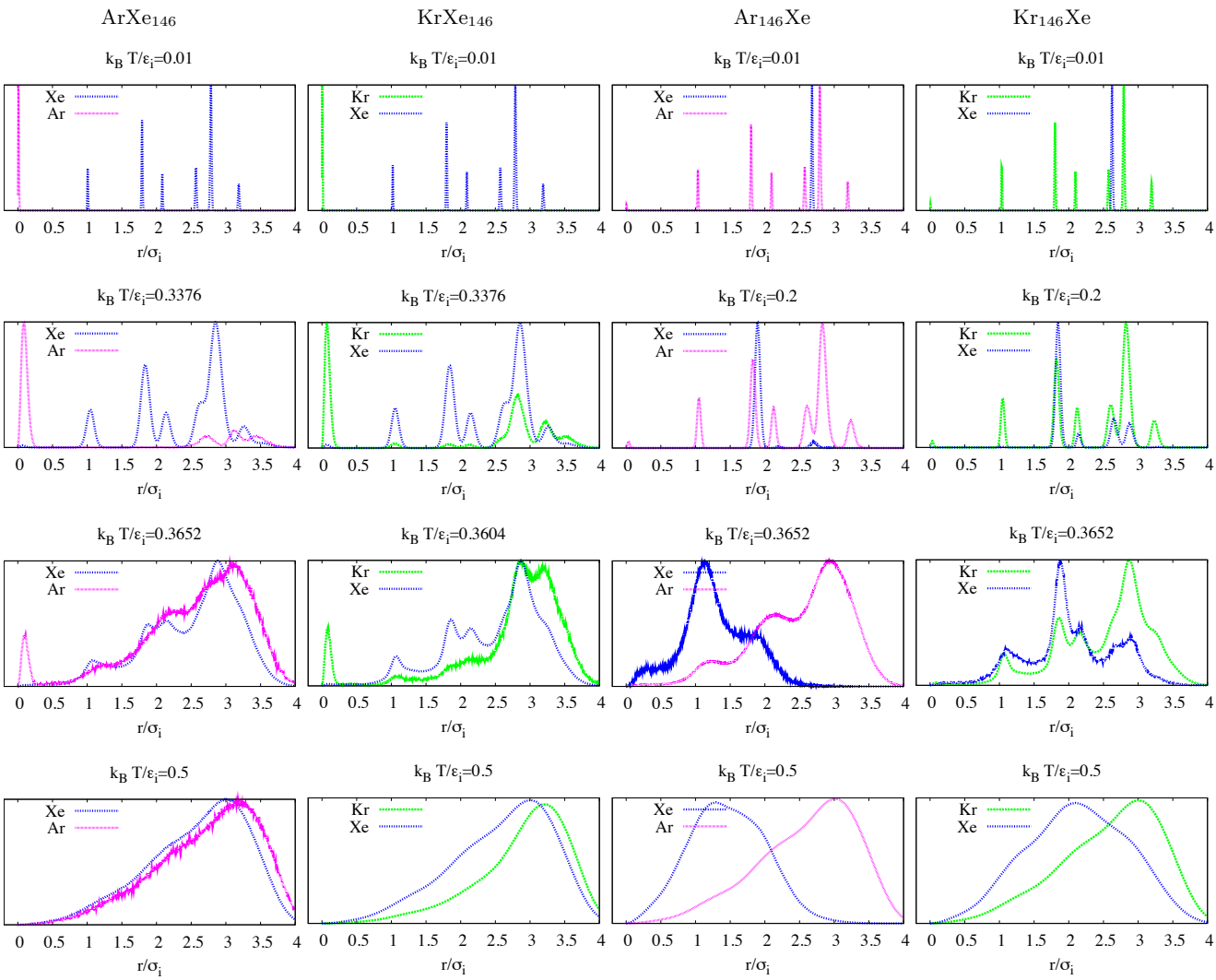

FIG. 7. (Color online) Radial distribution function for 147-atom clusters.

the order of the point group of the state α]. $\bar{\nu}_\alpha$ is the geometric *mean* vibrational frequency of each state (which is proportional to geometric mean of the square roots of the eigenvalues of the matrix $\hat{H}$) and N is the number of atoms considered.

III. RESULTS AND DISCUSSION

A. Size dependence of the melting temperature

In Fig. 2, we present the results of our calculations regarding the variation in the melting temperatures as a function of $N^{-1/3}$. It is seen that as the size of the cluster is increased the melting temperature of the clusters also increases, this behavior has been verified for Ar and Xe clusters.[24] The case of $N=13$ is certainly out of any linear tendency for all the compositions, yet, for other larger clusters $N=55,147,309$ where surface effects are less marked the dependence of the melting temperature as a function of $N^{1/3}$ can be well described by a line, and in all cases increases with the size of the cluster. From Fig. 2 is clearly seen that doping effects are very strong for small doped clusters ($N=13,55$), whose atoms have the highest differences between their LJ parameters, ϵ and σ (in this case argon and xenon). It is also seen that for the largest cluster sizes studied here their melting temperatures are almost equal for the doped and pure clusters.

B. Doping effects: Composition and size dependence

So far we have discussed the doping effects solely in terms of the position, on the temperature scale, of the peak associated with the melting of the cluster. Yet as is seen in Figs. 3 and 4 the peak changes, not only its position but also its height and width, for some compositions. For instance, for $Ar_{146}Xe$, the change in height with respect to Ar_{147} is noticeable although the displacement of the maximum is just around 1%. Other characteristic of the $C_V(T)$ that is modified by the presence of the dopant atom is the occurrence of a small peak or bump in the low-temperature region. As we will demonstrate in Sec. III C, for the clusters with sizes ($N=13,55,147$), this is due to a solid-solid transition. Some general trends for compositions $ArXe_{N-1}$ and $KrXe_{N-1}$ ($N=\{13,55,147,309\}$) are: regarding their lowest energy configurations, each pure Xe_N cluster and the doped $ArXe_{N-1}$ and $KrXe_{N-1}$ clusters have the same symmetry group (I_h),

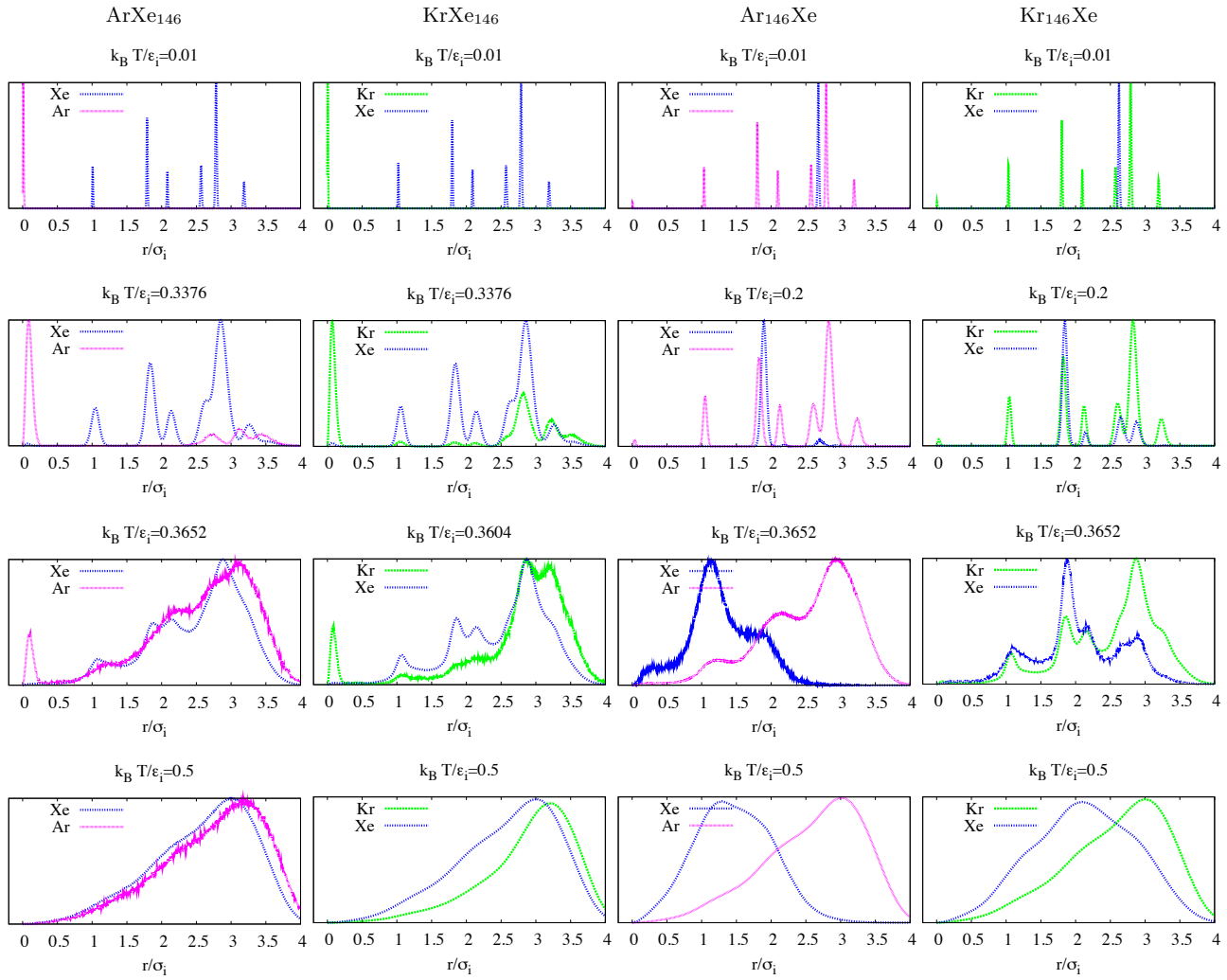

FIG. 8. (Color online) Radial distribution function for 309-atom clusters.

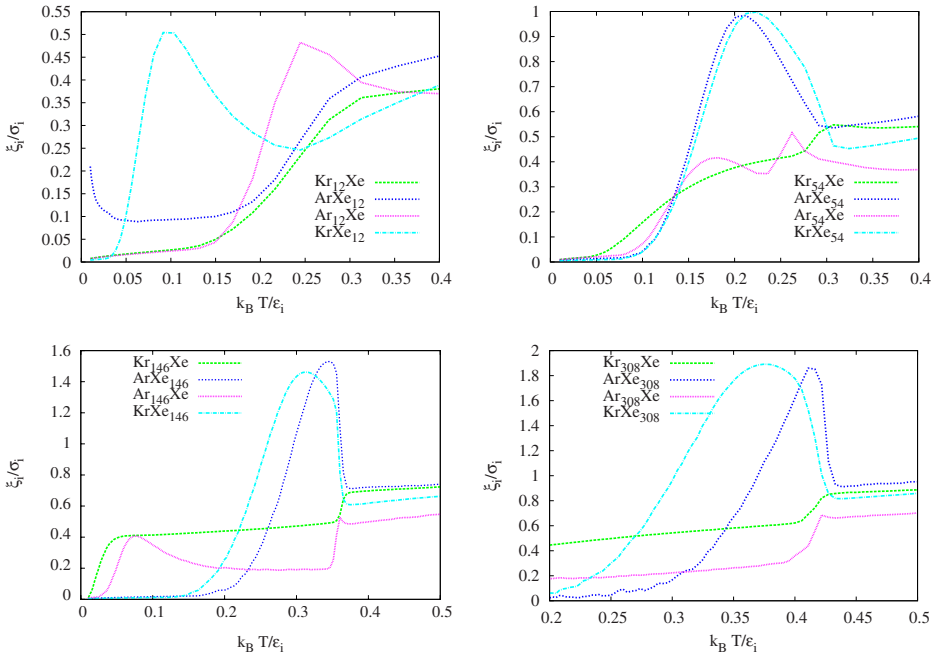

FIG. 9. (Color online) Standard deviation of the position of the dopant atom for cluster sizes (a) $N=13$, (b) $N=55$, (c) $N=147$, and (d) $N=309$.

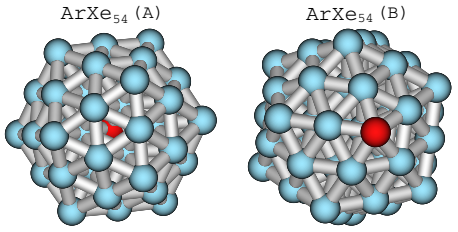

FIG. 10. (Color online) The two lowest energy configurations of $ArXe_{54}$. These configurations correspond to the lines labeled (A) and (B) in Fig. 12.

and are also very close in geometry. After a small temperature increase, the dopant atom in both $ArXe_{N-1}$ and $KrXe_{N-1}$ behaves the same way. It starts to move from the center of the cluster in the lowest energy configuration, to the second most energetically favorable position, in the outer shell of the cluster, as seen in the first two rows of Figs. 5–8. A pictorial representation of the process is given in Fig. 10. Nevertheless, excepting for the smallest cluster size, $N=13$, the dopant atom never relocalizes completely in a stable configuration different from the global minimum, this occurs because for larger structures $N>13$ there is more than one icosahedral stable structure in which the dopant atom is located in the outer shell of the clusters. To support this, see in Fig. 9 that, excepting for the cases $ArXe_{12}$ and $KrXe_{12}$, the standard deviation of the position of the dopant atom (ξ_{Xe}) is always an increasing function of the temperature, until the cluster melts. The bottom rows in Figs. 5–8 show that upon melting, the RDFs of the matrix and the dopant show the same structure. This indicates that, in the liquid phase, and for the compositions studied, Ar and Kr are not segregated by the Xe matrix. Finally, as one would expect based on the similarities of their LJ parameters, the Xe-Kr-doped clusters show more resemblance to the pure cluster in their C_V curves.

The clusters $Kr_{N-1}Xe$ are the ones that show a more similar behavior to the pure clusters LJ_N, considering their C_V curves. For these compositions, the standard deviation of the position of the dopant atom (ξ_{Xe}) is always an increasing function of the temperature (see Fig. 9). This implies that the Xe atom does not leave completely its external shell location, as in the lowest energy configuration (see the fourth column in Table I). Such configuration plays a significant role in the thermodynamics of the system until the phase change. This can be seen on the RDFs of Xe in the $Kr_{N-1}Xe$ clusters, as plotted in the fourth column of Figs. 5–8. Also, on the spectra of quenched energies of $Kr_{12}Xe$ and $Kr_{54}Xe$, in Figs. 11 and 12. The shape of ξ_{Xe} for $Kr_{N-1}Xe$ is qualitatively different depending on the cluster size N, indicating that the temperature ranges for the migration of the dopant atom and the melting of the cluster overlap for the smaller sizes. For $N=13$, ξ_{Xe} simply increases once the cluster starts to melt. For $N=55$, the dopant atom starts to delocalize smoothly between the second and first shells, until the migration is met by the melting of the cluster (see the last column in Fig. 6). For the largest structures $Kr_{146}Xe$ and $Kr_{308}Xe$, the dopant atom migrates to several positions in different shells of the structure, as seen in the last column of Figs. 7 and 8. Upon melting, these compositions show the same behavior observed in $ArXe_{N-1}$ and $KrXe_{N-1}$, i.e., there is no segregation between the Kr atoms and the Xe atom of

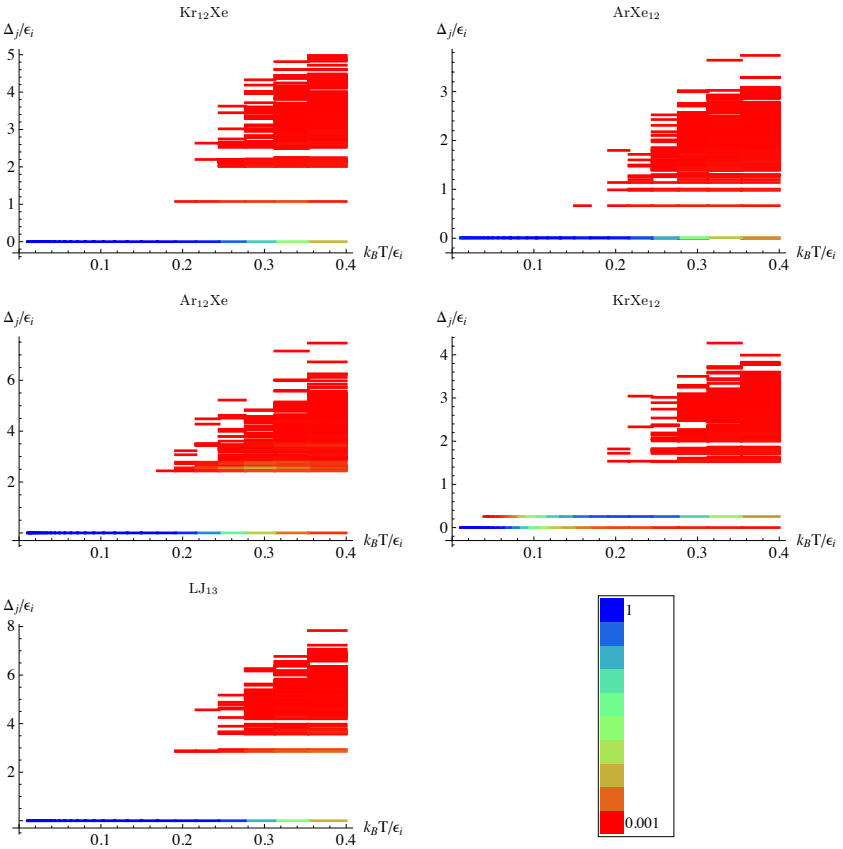

FIG. 11. (Color online) Spectra of quenched energies ($\Delta_j=E_j-E_0$) for 13-atom pure and doped clusters. The color indicates the relative sampling frequency of each minimum at a given temperature. Notice that the two lowest states of $ArXe_{12}$ overlap almost completely due to their small energetic difference.

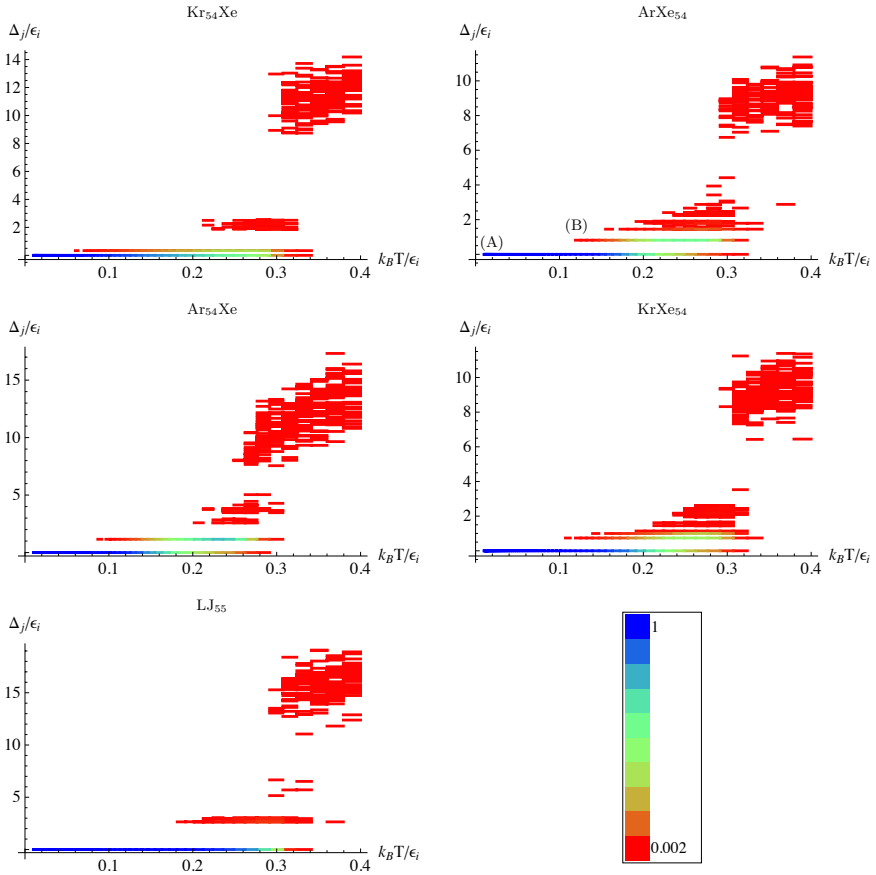

FIG. 12. (Color online) Spectra of quenched energies ($\Delta_j = E_j - E_0$) for 55-atom pure and doped clusters. The color indicates the relative sampling frequency of each minimum at a given temperature.

the cluster. The composition that shows more features during the heating process is $Ar_{N-1}Xe$. The largest doping effect is seen in the cluster $Ar_{12}Xe$. For this cluster we see that the melting temperature (taken as the position of the maximum in the $C_V(T)$ curve) drops by around $\Delta T = 0.037\epsilon_{Ar}/k_B$, which is around 13% of the melting temperature of the pure cluster. A comparable change in the melting point occurs for $Ar_{54}Xe$ with respect to Ar_{55}. This is not the only feature that changes drastically when replacing one atom, with respect to the melting of Ar_{55}. From Fig. 3 it is also seen that the melting peak in the $C_V(T)$ curve for the doped cluster is smaller, by almost a factor of 2, as compared with the pure cluster, in other words the latent heat associated with the melting is smaller in the doped cluster. The reduction in the latent heat is a feature present in all the argon clusters, doped with xenon. For the case of $Ar_{54}Xe$ two different transitions are seen in the RDF, $g(r)$, of the dopant atom (see the third column of Fig. 6). These transitions are seen in the nonmonotonous behavior of the standard deviation of the position of the Xe atom in Fig. 9. In the first transition, the Xe atom migrates from the outer shell to the inner shell, and remains there. As it was mentioned in the last section, this causes a small bump in the C_V curve. Then, as the temperature is further increased, the atom starts to migrate between the center of the cluster, the first shell and the outer shell. This occurs near the temperature range for the phase change. Finally, when the cluster reaches the liquidlike phase an interesting effect occurs, namely the Xe atom is segregated from the Ar atoms. This is clearly seen in the last row of Figs. 5–8. We note that, for all the cases studied, the segregation is related to a maximum size contrast between the impurity and other atoms in the cluster.

C. Low-*T* behavior

One of the most interesting features of the C_V calculations presented in Figs. 3 and 4 is the occurrence of a second small peak, not seen in the pure clusters, for some of the doped structures. The most noticeable case being that of $KrXe_{12}$. Such peak has been associated with a solid-solid transition, and studied in detail for rare-gas clusters of 6 (Ref. 25) and 13 (Refs. 26–30) atoms. It has been suggested[25–30] that this bump is due to structural transitions between isomers of the same composition. We reach the same conclusion via an analysis of around 1000 structures, which we sampled, for each replica and each composition in clusters with up to 147 atoms. We later quenched those structures. The energies and relative sampling frequencies of the set of minima obtained for each composition are presented in Figs. 11 and 12. From these figures we note that the extra peak correlates extremely well with the appearance of a second stable structure that becomes increasingly important until the cluster melts. This second structure corresponds to an icosahedron in which the dopant atom swaps positions with an atom in a different shell.

To further support our conclusion we have performed HSM calculations for some compositions. The input values used in the HSM calculations are shown in the first six columns of Table III. In the last column of the same table, we show the results (i.e., the predicted temperature for the solid-

TABLE III. Parameters used for the HSM. $\Delta/\epsilon_{\mathrm{Ar}}$ is the energy difference between the lowest energy structure and the second stable structure considered. Δ/ϵ_i is the scaled difference of the two levels considered in terms of the ϵ parameter of the matrix. The fourth column is the point group of the low-energy minimum. ν_i is the square root of the geometric mean of the nonzero eigenvalues of the Hessian Matrix $\hat{H}$ for each stable structure and $k_B T_h = \frac{\Delta}{(3N-6)\ln \bar{\nu}_0/\bar{\nu}_1 - \ln h_0/h_1}$ is the temperature at which the transition between the two solid structures is expected, i.e., at which the partition functions associated with each minimum are equal (Ref. 23).

Cluster	$\Delta/\epsilon_{\mathrm{Ar}}$	Δ/ϵ_i	Point group, second state	$\sigma_i^2\bar{\nu}_0/\epsilon_i$	$\sigma_i^2\bar{\nu}_1/\epsilon_i$	$k_B T_h/\epsilon_i$
$Kr_{12}Xe$	2.02627	1.47523	I_h	11.622	9.8675	0.50598
$ArXe_{12}$	0.04162	0.02247	C_{5v}	12.777	11.826	0.00446
$Ar_{12}Xe$	3.46358	3.46358	I_h	11.349	6.4721	0.21580
$KrXe_{12}$	0.87796	0.47406	C_{5v}	13.136	12.208	0.09668
$Kr_{54}Xe$	0.63580	0.46289	C_{5v}	13.032	12.844	0.15423
$ArXe_{54}$	2.79753	1.51055	C_{5v}	14.374	13.954	0.19544
$Ar_{54}Xe$	1.15348	1.15348	C_{5v}	12.544	11.919	0.14918
$KrXe_{54}$	2.53307	1.36775	C_{5v}	14.307	14.019	0.21457
$Ar_{146}Xe$	0.36404	0.36404	C_{2v}	13.519	13.381	0.08944

solid change associated with the transition between the two minima). The predicted temperatures agree well with those obtained from the PTMC simulations in Figs. 3 and 4. Table III also shows why the extra peak is not present in all clusters. For $Kr_{12}Xe$, $Ar_{12}Xe$, and $Kr_{54}Xe$, as can be seen in the insets of Fig. 3, the temperature of the solid-solid transition is so close to the melting peak, that when the structure can change to a different minima it has started to sample liquid-like configurations.

IV. CONCLUSIONS

PTMC simulations for rare gases (LJ) doped clusters with up to 309 atoms showed that a single atom impurity can cause doping effects such as the depletion of the melting range (with respect to the pure cluster), and the occurrence of a solid-solid transition in the low-temperature range.[31] The shifting of the melting range due to the presence of the single atom impurity decreases with increasing cluster size. In terms of absolute temperature it is noticeable for clusters with less than a 100 atoms, for instance for $Ar_{54}Xe$ it represents 3.4 K. Several criteria (i.e., C_V curves, radial distribution functions, spectra of quenched energies, and HSM) have been used to support that a solid-solid transition peak may arise for doped clusters with up to 147 atoms.

ACKNOWLEDGMENTS

We thank Fundación para la Promoción de la Investigación y la Tecnología del Banco de la República and Universidad de Antioquia for financial support, and CRESCA-SIU for computational resources. We also thank F. Calvo for helpful discussions and for providing the multihistogram method computer code.

*Corresponding author; gloria.moyano@exactas.udea.edu.co

[1] R. Ferrando, J. Jellinek, and R. L. Johnston, Chem. Rev. **108**, 845 (2008).
[2] F. Baletto and R. Ferrando, Rev. Mod. Phys. **77**, 371 (2005).
[3] J. P. K. Doye, D. J. Wales, and M. A. Miller, J. Chem. Phys. **109**, 8143 (1998).
[4] F. Calvo and F. Spiegelmann, J. Chem. Phys. **112**, 2888 (2000).
[5] F. Chen and R. L. Johnston, ACS Nano **2**, 165 (2008).
[6] E. G. Noya and J. P. K. Doye, J. Chem. Phys. **124**, 104503 (2006).
[7] H. Duan, F. Ding, A. Rosn, A. R. Harutyunyan, S. Curtarolo, and K. Bolton, Chem. Phys. **333**, 57 (2007).
[8] M. Wautelet, J. Phys. D **24**, 343 (1991).
[9] R. Vallée, M. Wautelet, J. P. Dauchot, and M. Hecq, Nanotechnology **12**, 68 (2001).
[10] A. A. Shvartsburg and M. F. Jarrold, Phys. Rev. Lett. **85**, 2530 (2000).
[11] C. Mottet, G. Rossi, F. Baletto, and R. Ferrando, Phys. Rev. Lett. **95**, 035501 (2005).
[12] C. Hock, S. Straßburg, H. Haberland, B. v. Issendorff, A. Aguado, and M. Schmidt, Phys. Rev. Lett. **101**, 023401 (2008).
[13] J. P. K. Doye and L. Meyer, Phys. Rev. Lett. **95**, 063401 (2005).
[14] F. Calvo and E. Yurtsever, Phys. Rev. B **70**, 045423 (2004).
[15] R. Topper, D. Freeman, D. Bergin, and K. LaMarche, Rev. Comput. Chem. **19**, 1 (2003).
[16] P. A. Frantsuzov and V. A. Mandelshtam, Phys. Rev. E **72**, 037102 (2005).
[17] D. J. Earl and M. W. Deem, Phys. Chem. Chem. Phys. **7**, 3910 (2005).
[18] D. Wales, J. Doye, A. Dullweber, M. Hodges, F. Naumkin, F. Calvo, J. Hernández-Rojas, and T. Middleton, *The cambridge cluster database*, http://www-wales.ch.cam.ac.uk/CCD.html
[19] D. J. Wales and J. P. K. Doye, J. Phys. Chem. A **101**, 5111 (1997).

[20] A. M. Ferrenberg and R. H. Swendsen, Phys. Rev. Lett. **63**, 1195 (1989).
[21] P. Labastie and R. L. Whetten, Phys. Rev. Lett. **65**, 1567 (1990).
[22] F. G. Amar and R. S. Berry, J. Chem. Phys. **85**, 5943 (1986).
[23] J. P. K. Doye and F. Calvo, Phys. Rev. Lett. **86**, 3570 (2001).
[24] E. Pahl, F. Calvo, L. Koccaroni, and P. Schwerdtfeger, Angew. Chem., Int. Ed. **47**, 8207 (2008).
[25] R. P. White, S. M. Cleary, and H. R. Mayne, J. Chem. Phys. **123**, 094505 (2005).
[26] D. D. Frantz, J. Chem. Phys. **105**, 10030 (1996).
[27] D. D. Frantz, J. Chem. Phys. **107**, 1992 (1997).
[28] D. Sabo, J. D. Doll, and D. L. Freeman, J. Chem. Phys. **121**, 847 (2004).
[29] D. Sabo, C. Predescu, J. D. Doll, and D. L. Freeman, J. Chem. Phys. **121**, 856 (2004).
[30] L. J. Munro, A. Tharrington, and K. D. Jordan, Comput. Phys. Commun. **145**, 1 (2002).
[31] The C_V curve of LJ_{309} shows considerably large peaks in the temperature range $0.39 < k_B T/\epsilon < 0.43$. These have been studied in detail by Noya and Doye (Ref. 6). They point out that prior to the melting there is complex structural transformation involving several processes such as surface roughening and the formation of structures with diverse symmetries.